Materials Research. 2021; 24(5): e20200527
DOI: https://doi.org/10.1590/1980-5373-MR-2020-0527

The Microstructure and Microscopic Mechanical Performance of Welded Joint for 9%Ni Steel Using Nickel-Based Filler Metal

Xiaoquan Li[a,]*, Yixing Chen[a], Benxing Hao[a], Yujun Han[a], Yajie Chu[a], Jianzhong Zhang[b]

[a] *Nanjing Institute of Technology, School of Materials Science and Engineering, Nanjing, Jiangsu 211167, China*
[b]*Jiangsu Fuermu Welding Industry Co., Ltd, Wuxi, Jiangsu 214443, China*

Received: November 18, 2020; Revised: July 7, 2021; Accepted: August 4, 2021.

Shielded metal arc butt welded joints for 9%Ni steel using nickel-based filler metal were analyzed by optical microscopy, scanning electron microscope, as well as transmission electron microscopy. The nanoindentation method was used to study the correlation between the structure and micromechanical properties of the fusion welded joint. The results show that there is a microstructural evolution from melted deposit to 9%Ni base steel. A significant coarse lath martensite-bainite mixture has been obtained in 9%Ni steel close to the fusion boundary while the retained austenite distributing in grain boundary of lath martensite has reduced to an undetectable level. In fusion boundary, an intermetallic layer has been observed which corresponds to the epitaxial growth of weld metal. The analysis of stress-strain behavior using nanoindentation shows that the heat-affected zone of coarse grains exhibits ductility loss and quantitative plastic deformation failure. The fusion boundary has the lowest value of yield stress while the coarse grained heat affected zone has the maximum value of yield stress.

Keywords: *9%Ni steel, welded joint, nickel-based alloy, microstructure, microscope mechanics, nanindentation.*

1. Introduction

With the increasing demand for liquefied natural gas (LNG), the 9% nickel steel has been widely used to provide a tough welded pressure vessel at -196°C without the need for postweld heat treatment. Owning to the addition of nickel as an austenite stabilizing element which results the ferrite-austenite transformation occuring at appreciably low temperature, the body centered cubic (bcc) ferritic crystal of 9%Ni steel exhibits higher strength and superior toughness at cryogenic temperature. In general, the most suitable choice for welding of 9%Ni steel is nickel-based filler metals which are face centered cubic crystalline structure and very dissimilar to low carbon 9%Ni steel in compositions[1-6]. It is now widely recognized that weld thermal cycling is detrimental to mechanical properties of base metal of 9%Ni steel for the coarse grained heat-affected zone and excessive welding dilution also affects the weld metal of nickel-based alloys. However, numerous studies have been showing that high-chromium nickel-based alloys were susceptible to hot cracking during welding. The reheated weld and heat affected zone of nickel-based alloys are highly susceptible to intergranular hot cracking, called ductility dip cracking (DDC)[7-12]

The inhomogeneity of microstructures and difference in chemical compositions in the welded joint can change the mechanical properties. Jang et al.[13] investigated the correlation between the microstructural and fracture characteristics in coarse grained heat-affected zones of 9%Ni steel with welding thermal simulation method. However, there are difficulties in direct extrapolation of the results to actual welded joints because some factors can not been considered. It is known that reliability of the whole welded joints is governed by each component such as base metal, weld metal, fusion boundary zone and coarse grained heat-affected zone. Unlike conventional tests, the nanoindentation test allows determining the local material properties in the indented region precisely. Efforts have been made to characterize the mechanical properties of microstructures in materials using nanoscale tools. Farias et al.[14] evaluated the microstructural characterization of Ni-based superalloy 625 clad welded on 9%Ni steel pipe for application in the oil and gas industry. The transition zone has been found which has high hardness and low toughness, and promotes failure of the component during service. Zhu and Xuan[15] used nanoindentation technique to investigate the correlation between mechanical properties and microstructure in heat-affected zone. Shen et al.[16] also compared maps of predicted hardness calculated from misorientation determination with maps of actual hardness by nanoindentation in nickel-based alloy 690. It was found that strength and strain hardening coefficient are microstructure dependent. In the same way, Zhao et al.[17] explored the nanoindentation behavior of the grain boundaries and grain interior in alloy 690. Cheng et al.[18] calculated the stress-strain curves to predict the elasto-plastic behavior of quenching and partitioning steels from the nanoindentation load-depth curves with the inverse method proposed by Dao et al.[19]. The results show that nanoindentation with the proposed inverse method can be a viable way in determining the

*e-mail: lixq@njit.edu.cn

individual phase properties in a complex multi-phase material with sub-micron microstructural features. Nanoindentation measurements were performed on a creep deformed nickel-based superalloy to study segregations on the dendrite scale and to measure mechanical properties of individual phases by Rehman et al.[20]. The microstructures and mechanical properties of individual phase were examined using combined microstructural analysis and nanoindentation by Chu et al.[21]. Rodriguez and Gutierrez[22] investigated the correlation between nanoindentation and tensile properties with experiments, reported that a linear relationship has be verified between the nanohardness and both the yield stress and the tensile stress of the material. Chen et al.[23], Maier et al.[24] and Pham et al.[25,26] analyzed the microstructural compositions in the weld zone of a structural steel using nanoindentation and optical microscopy including base metal, heat-affected zone and weld metal. It was shown that nanoindentation is acceptable in the verification microstructural compositions in steel at three different locations of the weld zone. Moreover the mechanical properties in an SM490 steel weld zone were tried to be determined by combining nanoindentation, tensile test, finite element analysis, and optical microscopy examination for individual zone[27]. Recently, Mao et al.[28] evaluated the overall yield strength of the weldment using a new microstructure-property relationship based on static nanoindentation. However, these above studies did not still make a detailed explanation of the relationship between the microstructure and mechanical properties of welded joint for 9%Ni steel using nickel-based filler metal.

2. Experimental Details

The shielded metal arc butt welding was employed as the welding method in this work. 9%Ni steel plates with thickness of 9 mm were used as base metal for the investigation and ENiCrMo-6 electrode with diameter of 3.2 mm was used as welding consumables. Before welding, the 9%Ni steel plates were cut into test pieces with size of 300×100 mm and V groove with angle of 60 degree was prepared. The nominal chemical compositions in percentage weight and mechanical properties for the 9%Ni base metal and deposited metal of ENiCrMo-6 were listed in Table 1 and Table 2. The weld was completed with a voltage of 24 V and a current of 200 A.

The cross-sections of welded joints were cut out, ground and polished which contain base metal (BM), coarse grained heat affected zone (CGHAZ), fusion boundary zone (FB) and weld metal (WM) regions. The microstructures of as-welded butt joints were evaluated with optical microscopy and scanning electron microscope (JSM-6360LV) with an energy dispersive x-ray detector. XRD analysing was employed for determine the phase. Transmission electron microscopy (TEM, JEOL JEM-2100HR) was used for observation of nano-sized grains and corresponding area diffraction patterns.

Nanoindentation tests were performed at room temperature using a Nano Indenter G200 made by Agilent Technologies Inc., USA[29,30]. Taking into account the inhomogeneity of the local mechanical response in welded joint, nanoindentation was performed in four regions, BM, CGHAZ, FB and WM. Before nanoindentation, Perform ultrasonic cleaning to remove oxide film and surface impurities (that was induced during mechanical grinding) of specimens. The maximum indentation load of 100 mN was applied to obtain the maximum penetration depth in the range of 800 nm to 1100 nm and then held constant for a dwell time of 20s. The subsequent unloading was also set to a rate of 0.05 mN/s.

To identify the fracture morphology for each individual regions, the longitudinal tensile specimens along weld length and transverse bending specimens were prepared as schematically illustrated in Figure 1. The width of tensile specimens was enough to include the fracture locations of BM, CGHAZ, FB and WM. In this way, it is possible to obtain the different fracture morphology of all regions in the same tensile specimens. The transverse bending test can be used to observe the appearance of the fracture of the center weld.

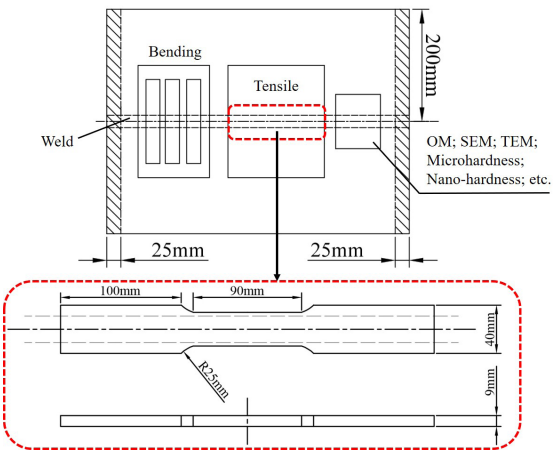

Figure 1. Sampling diagram.

Table 1. Chemical compositions of the 9%Ni steel and deposited metal of ENiCrMo-6(in wt,%).

Materials	C	Mn	P	S	Si	Cr	Mo	Fe	W	Nb+Ta	Ni
9%Ni	0.021	0.72	0.002	0.003	0.25	-	-	Bal.	-	-	9.18
ENiCrMo-6	0.01	3.02	0.003	0.005	0.37	14.22	5.72	5.80	1.66	0.86	Bal.

Table 2. Mechanical properties of 9Ni% steel and deposited metal of ENiCrMo-6.

Materials	Yield stress ReL / MPa	Tensile stress Rm/ MPa	Elongation δ%	Notch impact toughness (-196°C) AKV / J
9%Ni steel	703	727	25.9	223
ENiCrMo-6	680	410	40	130

3. Results and Discussion

3.1 Microstructural characteristics of welded joint

The optical micrographs of welded joint for weld metal (WM or fusion zone), fusion boundary (FB) and coarse grained heat affected zone (CGHAZ) are shown in Figure 2a-c and base metal (BM) of 9%Ni steel in Figure 2d. The general austenite solidification structure can be observed in weld deposit (Figure 2a). The precipitates distributing with dispersion in the interior of austenite grain are also evident. Figure 2b, c illustrates the obvious columnar grains from the edge of solid base metal to weld centre in fusion boundary, while a significant coarse lath martensite-bainite mixture which is caused by peak temperature of over 1100°C during weld thermal cycling has been obtained in solid metal close to the fusion boundary. Obviously, there is a microstructure change from solid metal to molten deposit. Since the weld metal is rather dissimilar to base metal in compositions and microstructure, the microstructure evolution can be quite complex. At the high temperature, both 9%Ni steel and nickel-based weld metal have an fcc crystalline structure. Therefore, it was expected that the liquid weld pool, in contact with the partially molten substrate, would rearrange with the same crystallographic orientation (epitaxia nucleation). A tiny epitaxial growth of weld metal which initiates from the substrate was found in Figure 2b. Since this epitaxial growth was initiated by arranging atoms from the liquid nickel-based metal on the existing crystalline substrate, thereby extending the grain of solid 9Ni% steel without altering the crystallographic orientation of bcc despite of martensitic transformation of substrate. There has been known that the columnar grains of weld metal are the face centered cubic crystal structure and grow in the direction perpendicular to the fusion boundary due to maximum temperature gradient and thus the maximum driving force for solidification. Although the weld deposit of nickel-based alloy is different from base metal of 9%Ni steel in crystalline structure, whether face-centered-cubic (fcc) or body-centered-cubic (bcc) have the same <100> preferred direction of growth. Therefore, both the epitaxial growth and columnar grain growth will grow more easily in direction with their easy growth direction (i. e. <100>) parallel to the direction of the maximum temperature gradient. It is anticipated that based on the crystalline structure differences, the crystal morphology differences would be evident. In addition, compared with Figure 3, the retained austenite distributing in grain boundaries of lathe martensite which is widely known as one of the most important factors affecting the cryogenic toughness has reduced to an undetectable level. According to XRD measurement by Jang et al.[13] with welding thermal simulation for 9Ni steel, the average volume fraction of retained austenite in the areas near the fusion line was less than 1%. Whereas 9%Ni steel generally consists of tempered martensite along with 5% retained austenite resulting from the full heat-treatment.

To observe the microstructural evolution from solid metal to melted deposit, SEM images at 1000× magnification and TEM micrographs were analyzed to determine detailed microstrure of fusion boundary. As shown in Figure 4, it is interesting to note that there is an intermetallic layer which is

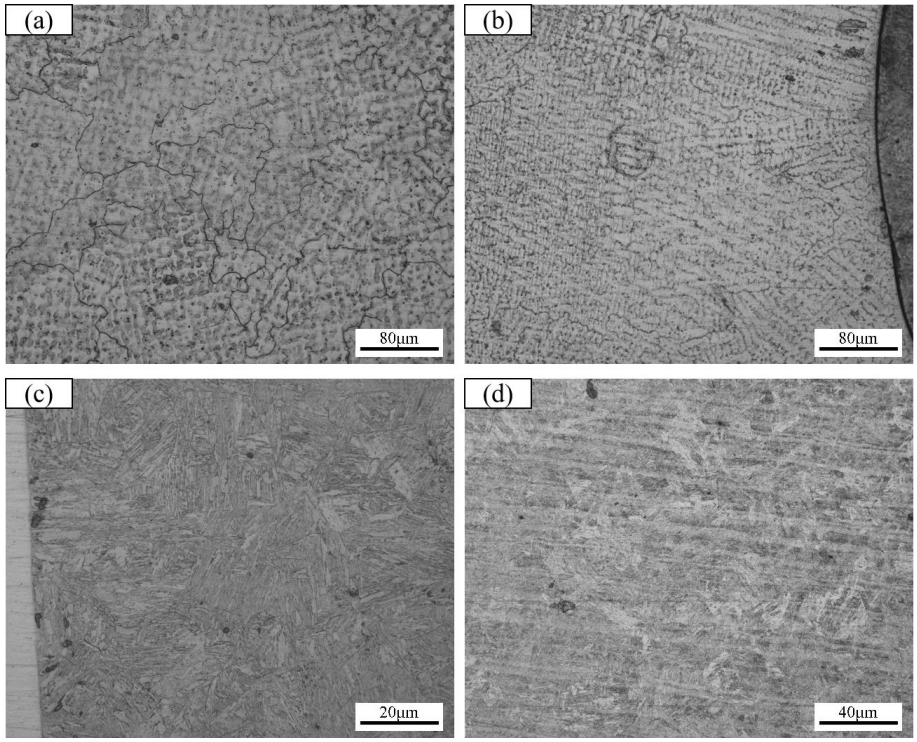

Figure 2. Metallographic structure of welded joint.

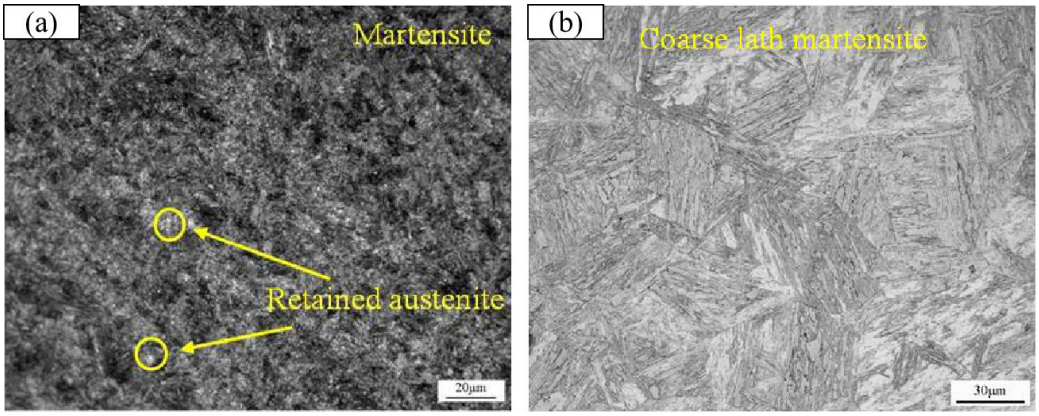

Figure 3. Comparison of base metal and inverted martensite in the coarse-grained region.

4-6μm in width between solid metal and melted deposit with SEM image. The composition profiles in the analytical electron microscope across the fusion boundary indicate that the layer exactly responds to position of iron element diffusing from weld deposit to solid metal and nickel or chromium elements in reverse direction. Therefore the intermetallic layer mainly consists of Ni-Fe-Cr-Mo multi-phase compositions which is very different from weld metal in compositions. According to Ni-Fe, Ni-Cr[31] and Ni-Mo[32] binary phase diagrams, the infinite solid solution of Ni-Fe, Ni-Cr can be formed at high temperature. While as cooling to room temperature or below, several intermetallic compounds such as Fe_3Ni, FeNi or $FeNi_3$ could precipitate from the solution. The XRD diffraction pattern of Fe-Ni as well as Ni-Cr intermetallic compounds in fusion boundary can be clearly identified as shown in Figure 5 The formation of intermetallic layer could be explained as following: The melted substrate was carried into the weld pool, where it solidified quickly due to the stagnation of the liquid next to the solid (or semi-solid) wall of the HAZ. This process allowed low chemical diffusion between substrate and melted filler metal. Generally, due to the diffusion of Ni, Cr, Mo and other elements, the mechanical properties of these intermetallic compounds are different from weld deposits or solid metals. The morphology of fusion boundary was further characterized using TEM. Typical TEM morphology of fusion boundary is presented as Figure 6 and Figure 7. It indicates that at the fusion boundary the 9%Ni steel consists of parallel oriented lath martensite with about 150nm width and lath martensites have been embedded into fusion zone. Since only the solid 9%Ni steel consists of lath martensite, this position is actually the solid/liquid interface and should corresponds to the epitaxial growth of weld metal. The TEM analysis revealed that close to the epitaxial growth, a higher density dislocation could be observed in bulk of the weld which corresponds to evolution from epitaxial growth (bcc) to column grain (fcc). This can be clarified by corresponding diffraction patterns for different microzones as shown in Figure 7.

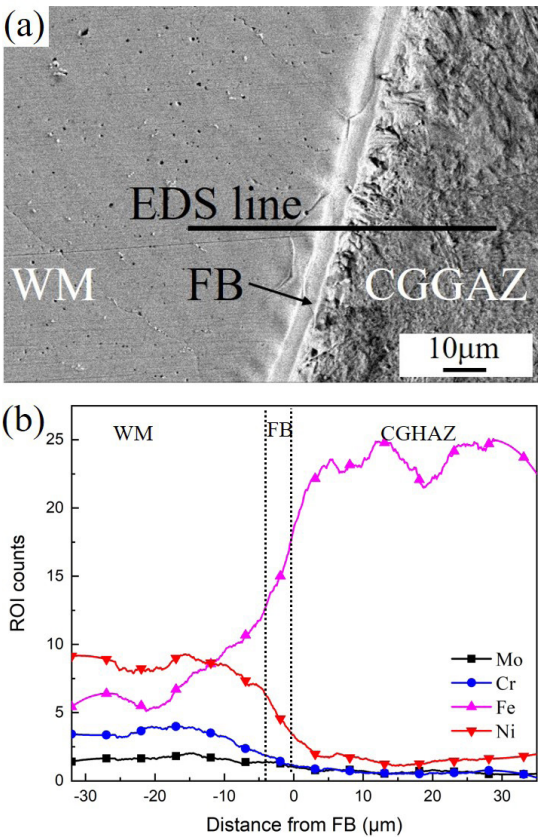

Figure 4. SEM and line scan of fusion zone.

3.2 Microscopic mechanical performance with nanoindentation

The average load-penetration depth (p-h) curves measured from the three indentation series in BM, CGHAZ, FB and WM are presented in Figure 8. In terms of the experimental p-h curves of BM, CGHAZ, FB as well as WM, the variation in depths is evident due to microstructural inhomogeneity and compositional dissimilarity. Under the same loading, the WM region exhibits the maximum penetration whereas the CGHAZ region the minimum and then the FB. Both the CGHAZ and the FB are lower than BM. Compared with the coarse grained heat affected zone, a fewer variation of penetration depth exits between FB and BM. The nanoindentation behavior provides some insights of microscopic mechanical performance for various regions of welded joint. The ratio

of maximum penetration depth for CGHAZ, FB, as well as WM to BM are summarized in Table 3. Note that, the CGHAZ is usually 83%-86% of BM. It indicates that the plastic deformation capacity of CGHAZ is only 83-86% of BM. Therefore, a quantitative plastic deformation damage is exhibited for coarse grain heat affected zone due to weld thermal cycling.

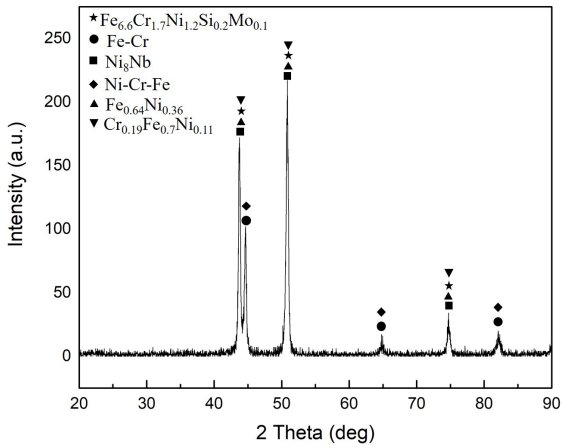

Figure 5. XRD of fusion zone.

Figure 9 shows the experimental curves of displacements versus time during holding constant for 20s in various regions which are related to dynamic characteristics of plastic flow. The corresponding Young's elastic modulus and nanohardness calculated by the Oliver-Pharr method across of the welded joint are illustrated in Figure 10. It can be seen that a distinct variation exits in various regions after initial constant loading for about 2s (seen in Figure 9). The fusion boundary has the lowest values of both hardness and elastic modulus while the the highest nanohardness value is in CGHAZ and so is the elastic modulus in BM. The values of FB and CGHAZ are about 77% and 111% that of BM respectively. The elastic modulus value of weld metal is lower than that of base metal and there is relatively little difference between CGHAZ and BM. It is easily understood for CGHAZ due to coarse grained structure. The phenomenon of the lower elastic modulus value in weld metal could be explained by nickel based composition which could form face centered cubic crystal structure. Although the crystal structure atoms

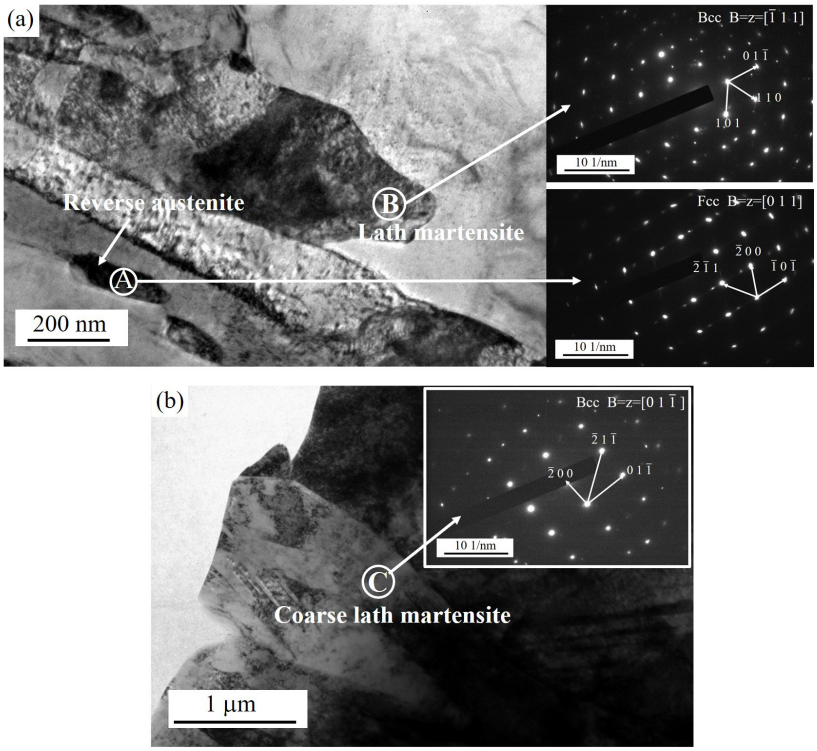

Figure 6. TEM base material and martensite in the coarse-grained region reverse transformed austenite.

Table 3. Average of the maximum penetration depth and the ration to base metal.

Position	Weld Metal (WM)	Fusion Boundary (FB)	Coarse Grained Heat Affected Zone CGHAZ	Base Metal (BM)
The maximum penetration depth	1075/1020	965/840	880/800	1020/970
Ration of maximum penetration depth to base metal	105%/93%	95%/87%	86%/83%	——

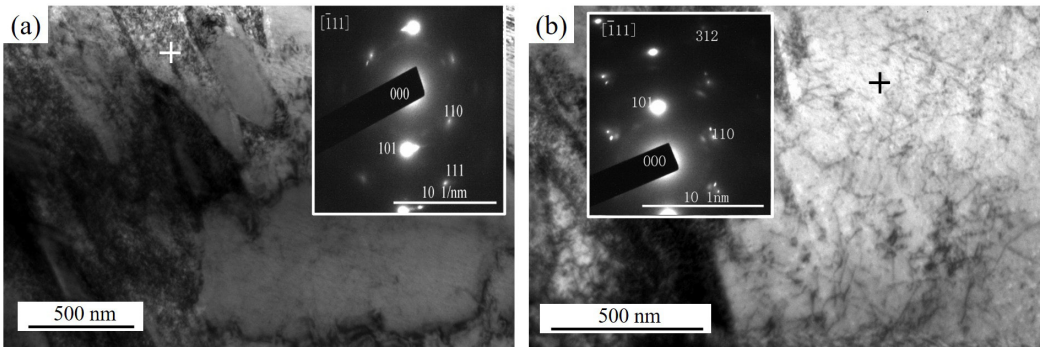

Figure 7. TEM and diffraction spots in the fusion zone.

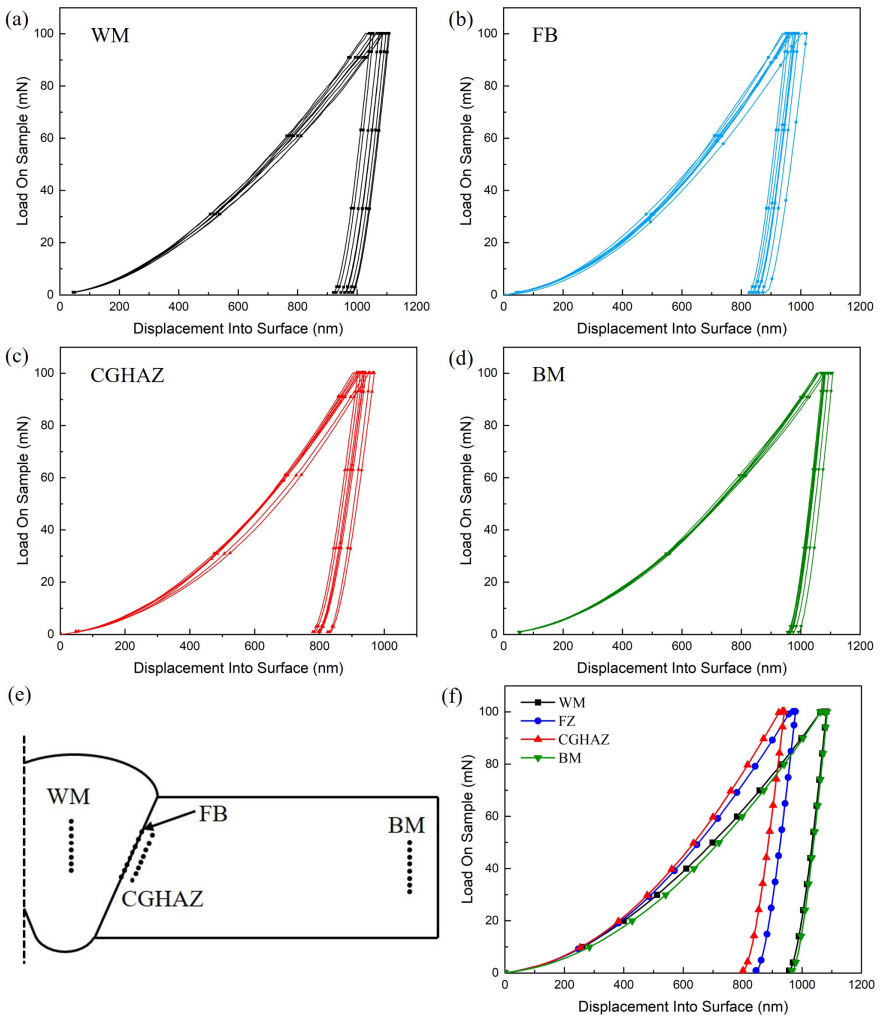

Figure 8. P-h curve of each micro área.

of the face-centered structure can be hardened through solid solution or other mechanisms, there is a chemical gradient between the nickel-based weld metal and the 9% Ni steel at the fusion boundary, this causes the Fe atoms in the molten 9% Ni-based metal to diffuse between the metals, resulting in the formation of a diffusion zone. The experiment found that the hardness and elastic modulus at the fusion boundary are both the lowest. The dissimilar nickel-based metal welds for low-alloy steel have been investigated by Choi et al.[33] and the effects of thermal aging treatment on the low-alloy steel side near the fusion boundary would result of the formation of Cr-rich precipitates, $Cr_{23}C_6$ etc.. As analyzed earlier, the epitaxial growth at fusion boundary always initiates from the body centered cubic crystal structure of 9%Ni base metal without altering the crystallographic orientation. Note that the elastic modulus is largely dependent on chemical compositions

of material while has nothing with microstructure. Thus this also verifies there exists an intermetallic layer at fusion boundary. Moreover, the curves of displacements versus time during holding constant illustrate that the fusion boundary and coarse grained heat affected zone have a lower capacity of plastic flow than base metal or weld metal.

Based on the above experimental results, it can be concluded that the two weaker connection areas of the welded joint are affected by the different grain sizes and element diffusion, and the microscopic elastic modulus and nanometer value of the coarse-grained heat-affected zone and different hardness performance in the boundary area of the fusion line

3.3 Fracture behavior of welded joint

Figure 11 shows the SEM fractures morphologies of welded joint in longitudinal tensile which includes each individual weld zone at room temperature. In the meantime, the fracture morphology of transverse bending section of weld is showed in Figure 12. As shown in Figure 11, a typical ductile fracture, but each individual weld zone with difference morphology are distinctly seen. Especially, the intermetallic layer of fusion boundary could be evidently observed. In contrast to 9%Ni base metal, the dimples of fractured tensile specimen in CGHAZ only exhibits slightly larger in size and more inhomogeneous distribution.

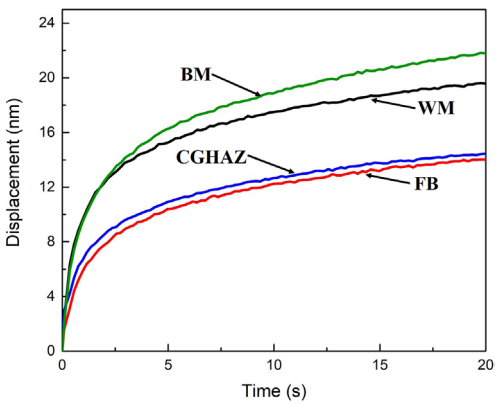

Figure 9. Variation curve of indentation depth with time.

It indicates that there is not too much influence of hardening in CGHAZ on fracture behavior for 9Ni% steel welded joint in spite of grain growth severely due to weld thermal cycling. The weld metal fracture surface shows a mixture of dimple and quasi cleavage. Some brittle fracture features on weld metal adjacent to fusion boundary have been revealed and the microcracks initiate at this brittle region have been detected. For cross-section of the weld metal, the appearance of fractured tensile specimen could show obviously the direction of columnar grains which are parallel to each other. The difference in chemical composition between dendrites and dendrites causes different fracture modes. However, as shown in Figure 12, this appearance can not be observed in fracture of bending specimen which is fractured in weld metal center with equiaxed grains. It is interesting to note in Figure 11 that the fracture morphology in FB is clearly different when compared with that in WM or BM. In this region, a special tearing ridge becomes dominating fracture mode. The explanation for this may be uneven deformation during stretching. As measured above, the fusion boundary located at the interface of solid/liquid has the lowest values of both hardness and elastic modulus. Therefore, under the same tensile action in the two regions of BM and WM, the plastic deformation will be preferentially concentrated on the solid/liquid fusion boundary with lower hardness, and eventually a large number of tear ridges will be formed. In general, the material's stress-strain behavior can be fully described with the parameters of hardness H, modulus E, yield stress σ_y, and hardening exponent n. In view of this consideration, the empirical relationship between nanohardness and yield strength reported in literature[17,18] was introduced to estimate yield strength. The material's elasto-plastic behavior can be described as:

$$\begin{cases} \sigma = E\varepsilon & for \quad \sigma \le \sigma_y \\ \sigma = \sigma_y \left(1 + \dfrac{E}{\sigma_y}\varepsilon_p\right)^n & for \quad \sigma > \sigma_y \end{cases} \tag{1}$$

Where ε_p is the nonlinear part of the total strain ε, accumulated beyond the yield strain ε_y, and defined as $\varepsilon_p = \varepsilon - \varepsilon_y$.
and hardening exponent *n* can be described as:

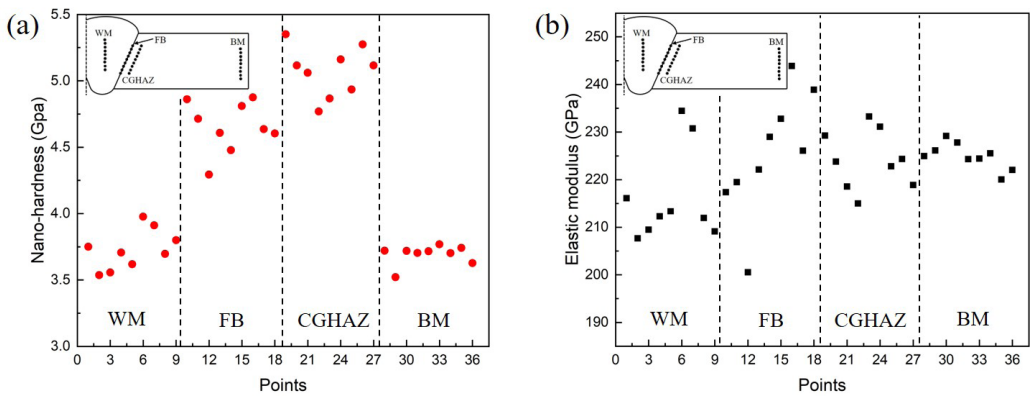

Figure 10. Nano hardness and elastic modulus distribution.

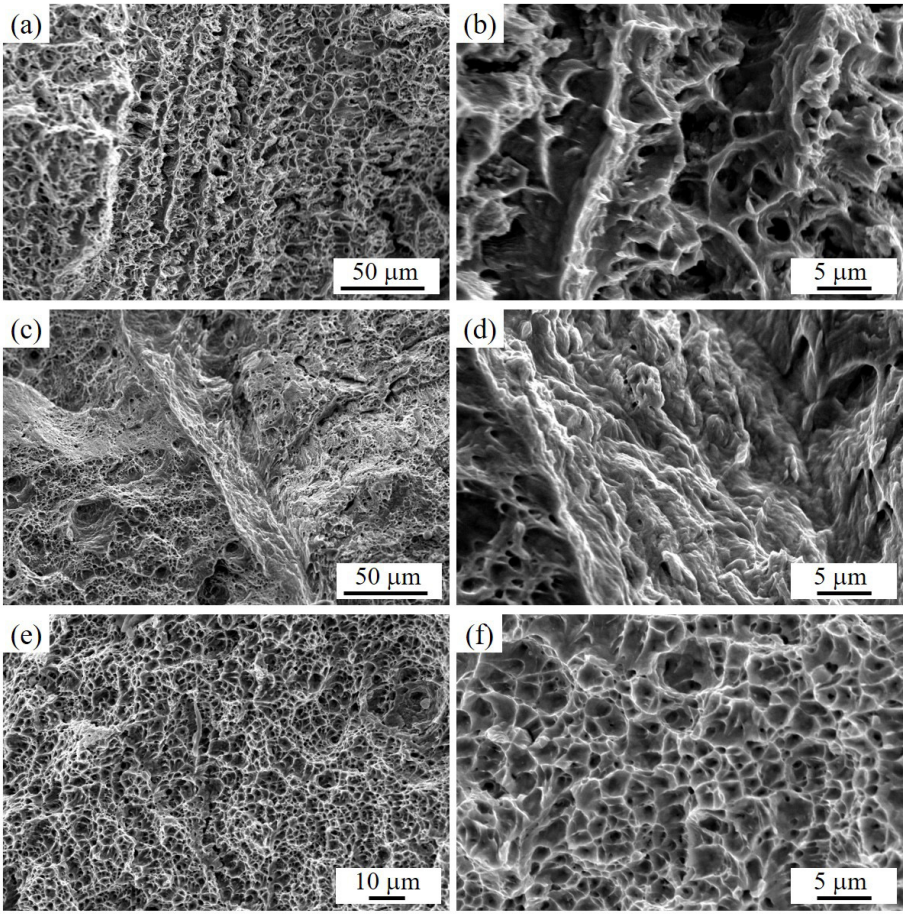

Figure 11. SEM fracture morphology of each micro área.

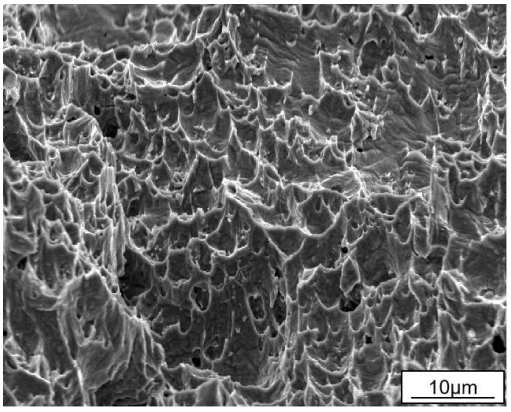

Figure 12. Fracture morphology of weld center.

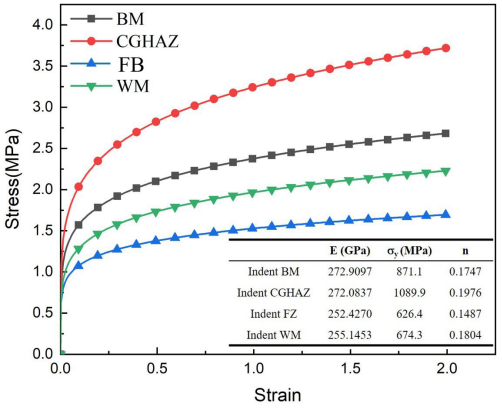

Figure 13. Stress-strain curve of each micro área.

$$n=\log\frac{\sigma_{0.033}}{\sigma_y}\Big/\left(1+0.033\frac{E}{\sigma_y}\right) \quad (2)$$

Considering the deep indentation on depths were adopted in the current study, i. e, 1600μm, the Indentation Size Effect (ISE) could be neglected which is only strongly dependence on the indentation depth of no more than 100nm. With the inverse method which enables the extraction of stress-strain curves proposed by Dao et al.[19] and other researchers[18,22,34]. and the determination of hardening exponent n, the stress-strain curves calculated based on parameters for BM, CGHAZ, FB as well as WM regions are illustrated in Figure 13. It shows that the fusion boundary has the lowest value of yield stress σ_y while the coarse grained heat affected zone the maximum.

4. Conclusions

In the fabrication of LNG storage tanks and vessels with 9%Ni steel, the weld zone is usually considered as "weakest link" due to weld defects and microstructural inhomogeneity. In this study, the welded joints for 9% Ni steel using nickel-based filler metal were analyzed by optical microscopy, scanning electron micrscope as well as transmission electron microscopy. The microstructural evolution from melted deposit to 9%Ni base steel has been revealed. A significant coarse lath martensite-bainite mixture has been obtained in 9%Ni steel close to the fusion boundary while the retained austenite distributing in grain boundary of lath martensite has reduced to an undetectable. In fusion boundary, an intermetallic layer has been observed which corresponds to the epitaxial growth of weld metal. The inhomogeneity of the weld zone structure may lead to changes in mechanical properties, so that the weld zone and the rest of the weld have layers with different mechanical resistances, causing the area to produce heterogeneity in plastic deformation, and eventually stress concentration may occur at the weak point. The nanoindentation technique which allows very small regions to be investigated was used for the investigation of microstructures and mechanical properties of the joint including weld metal zone, fusion boundary zone, coarse grained heat affected zone and base metal. The distributions of mechanical properties for every small individual region, such as elastic modulus E, hardness H, yield strength σ_y and strain hardening explonent n, across the weld znoe were determined. This made it possible to evaluate the mechanical and micropstructure properties of inhomogeneous welded joint. The stress-strain behavior analyze using nanoindentation show that a quantitative plastic deformation damage is exhibited for coarse grain heat affected zone. The fusion boundary has the lowest value of yield stress while the coarse grained heat affected zone has the maximum value of yield stress.

5. Acknowledgements

This research work is supported by the Primary Research and Development Plant of Jiangsu Province (BE2017168). We thank Yujie Ma (Collaborative Innovation Center of Advanced Microstructures, Nanjing University) for support in preparation of TEM samples and implementation of experiments.

6. References

1. Nako H, Okazaki Y, Takeda H, Suenaga K, Nakanishi K. Comparison of microstructures at as welded zone in 9%Ni steel similar composition weld metal. Mater Sci Forum. 2010;638-642:3693-8.
2. Kobelco. Kobelco's welding consumables for LNG storage tanks made of 9% ni Steel. Kobelco Weld Today. 2011;14(2):3-8.
3. El-Batahgy AM, Gumenyuk A, Gook S, Rethmeier M. Comparison between GTA and laser beam welding of 9% Ni steel for critical cryogenic applications. J Mater Process Technol. 2018;261:193-201.
4. Yoon Y-K, Kim J-H, Shim K-T, Kim Y-K. Mechanical characteristics of 9% Ni steel welded joint for LNG storage tank at cryogenic. Int J Mod Phys Conf Ser. 2012;6:355-60.
5. Khourshid AEFM, Ghanem MA. The influence of welding conditions on mechanical properties of 9% Ni steel welded joints of liquefied natural gas tank. Int J Eng Sci. 2013;2(1):179-85.
6. Ahsan Q, Haseeb ASMA, Syahriah NI, Chang SY. 9% Nickel steels and their welding behavior. Comprehensive Materials Processing. 2014;6:135-49.
7. Ramirez J, Lippold JC. High temperature behavior of Ni base weld metal. Part II. Mater Sci Eng A. 2004;380(1-2):245-58. http://dx.doi.org/10.1016/j.msea.2004.03.075.
8. Fink C. An investigation on ductility-dip cracking in the base metal heat-affected zone of wrought nickel base alloys-part I: metallurgical effects and cracking mechanism. Weld World. 2016;60(5):939-50.
9. Nissley NE, Lippold JC. Ductility-dip cracking susceptibility of nickel-based weld metals, Part I: strain-to-fracture testing. Weld J. 2008;87:257s-64s.
10. Nissley NE, Lippold JC. Ductility-dip cracking susceptibility of nickel-based weld metals: part II. Microstructural characterization. Weld J. 2009;88:131s-40s.
11. Collins MG, Lippold JC. An investigation of dutility dip cracking in nickel-based filler materials, Part I. Weld J. 2003;10:288s-95s.
12. Sham K, Liu S. Flux-coating development for SMAW consumable electrode of high-nickel alloys. Weld J. 2014;93:271s-81s.
13. Jang J, Ju J-B, Lee B-W, Kwon D, Kim W-S. Effects of microstructural change on fracture characteristics in coarsegrained heat-affected zones of QLT-processed 9% Ni steel. Mater Sci Eng A. 2003;340(1-2):68-79.
14. Farias FWC, Payão JC Fo, Silva DA Jr, Moura RN, Rios MCG. Microstructural characterization of Ni-based superalloy 625 clad welded on a 9% Ni steel pipe by plasma powder transferred arc. Surf Coat Tech. 2019;374:1024-7. http://dx.doi.org/10.1016/j.surfcoat.2019.06.084.
15. Zhu ML, Xuan FZ. Correlation between microstructure, hardness and strength in HAZ of dissimilar welds of rotor steels. Mater Sci Eng A. 2010;527(16-17):4035-42.
16. Shen RR, Ström V, Efsing P. Spatial correlation between local misorientations and nanoindentation hardness in nickel-base alloy 690. Mater Sci Eng A. 2016;674:171-7.
17. Zhao Y, Choi I-C, Kim Y-J, Jang J. On the nanomechanical characteristics of thermally-treated alloy 690: grain boundaries versus grain interior. J Alloys Compd. 2014;582:141-5.
18. Cheng G, Choi KS, Hu X, Sun X. Determining individual phase properties in a multi-phase Q&P steel using multi-scale indentation tests. Mater Sci Eng A. 2016;652:384-95.
19. Dao M, Chollacoop N, Van Vliet KJ, Venkatesh TA, Suresh S. Computational modeling of the forward and reverse problems in instrumented sharp indentation. Acta Mater. 2001;49(19):3899-918.
20. Rehman H, Durst K, Neumeier S, Parsa AB, Kostka A, Eggeler G, et al. Nanoindentation studies studies of the mechanical properties of the phase in a creep deformed Re containing nickel-based superalloy. Mater Sci Eng A. 2015;634:202-8.
21. Chu Q, Bai R, Zhang M, Li J, Lei Z, Hu N, et al. Microstructure and mechanical properties of titanium/steel bimetallic joints. Mater Charact. 2017;132:330-7.
22. Rodriguez R, Gutierrez I. Correlation between nanoindentation and tensile properties Influence of the indentation size effect. Mater Sci Eng A. 2003;361(1-2):377-84.
23. Chen S, Ye X-X, Yu K, Li C, Li Z, Li Z, et al. Microstructure and mechanical properties of UNS N10003 alloy welded joints. Mater Sci Eng A. 2017;682:168-77.
24. Maier P, Richter A, Faulkner RG, Ries R. Application of nanoindentation technique for structural characterisation of weld materials. Mater Charact. 2002;48(4):329-39.
25. Pham T-H, Kim JJ, Kim S-E. Estimation of microstructural compositions in the weld zone of structural steel using nanoindentation. J Construct Steel Res. 2014;99:121-8.

26. Pham T-H, Kim S-E. Nanoindentation for investigation of microstructural compositions in SM490 steel weld zone. J Construct Steel Res. 2015;110:40-7.
27. Pham T-H, Kim S-E. Determination of mechanical properties in SM490 steel weld zone using nanoindentation and FE analysis. J Construct Steel Res. 2015;114:314-24. http://dx.doi.org/10.1016/j.jcsr.2015.08.014.
28. Mao K, Wang H, Wu Y, Tomar V, Wharry JP. Microstructure-property relationship for AISI 304/308L stainless steel laser weldment structural materials: properties, microstructure and processing. Mater Sci Eng A. 2018;721:234-43.
29. Oliver WC, Pharr GM. An improved technique for determining hardness and elastic modulus using load and displacement sensing indentation experiments. J Mater Res. 1992;7(6):1564-83.
30. Oliver WC, Pharr GM. Measurements of hardness and elastic modulus by instrumented indentation: advance in understanding and refinements to methodology. J Mater Res. 2004;19(1):3-20.
31. Nash P. Ni-Cr system, phase diagrams of binary nickel alloys. Ohio: ASM International; 1991.
32. Singleton MF, Nash P. Ni-Mo system, phase diagrams of binary nickel alloys. Ohio: ASM International; 1991.
33. Choi KJ, Kim T, Yoo SC, Kim S, Lee JH, Kim JH. Fusion boundary precipitation in thermally aged dissimilar metal welds studied by atom probe tomography and nanoindentation. J Nucl Mater. 2016;471:8-16.
34. Iracheta O, Bennett CJ, Sun W. Characterization of material property variation across an inertia friction welded CrMoV steel component using the inverse analysis of nanoindentation data. Int J Mech Sci. 2016;107:253-63.